Intracellular dynamics of CA3 pyramidal cells underlie changes in firing output during theta and large irregular activity

Meryl Malezieux[1,2]*, Ashley L. Kees[1,2]* and Christophe Mulle[1,2,3]

[1]Interdisciplinary Institute for Neuroscience, CNRS UMR 5297

[2]University of Bordeaux, F-33000 Bordeaux, France

**equal contribution*

[3]Lead contact; correspondence: christophe.mulle@u-bordeaux.fr

Abstract

The hippocampal CA3 subregion integrates multimodal information processed in the entorhinal cortex and is important for rapid memory encoding. Different behaviors are correlated with distinct brain states characterized by specific oscillations in the hippocampal local field potential (LFP). Large Irregular Activity (LIA) is present during quiet wakefulness, and theta oscillations are present during exploratory behaviors. To support the various functions of CA3, its pyramidal cells (PCs) must change their activity depending on the brain state of the animal. To better understand the dynamic relationship between network and single-cell properties in CA3, we have made simultaneous whole-cell patch-clamp and LFP recordings during brain states occurring spontaneously in awake head-fixed mice free to run on a wheel. During theta, most CA3 PCs hyperpolarize, have lower amplitude subthreshold fluctuations, and reduce their firing rate. In contrast, during LIA, CA3 PCs have larger amplitude subthreshold fluctuations, tend to depolarize and increase their firing rate. These intracellular dynamics highlight single-cell state-dependent changes in the CA3 network, ensuring optimal integration and transfer of information.

Introduction

Wakefulness is comprised of distinct brain states, correlated with different behaviors and characterized by specific oscillatory patterns in the local field potential (LFP). The ability of brain circuits to perform the different computations that give rise to different behaviors is thought to rely upon state-dependent modulations in single-cell properties, such as resting membrane potential, spike threshold, and synaptic efficacy (Marder et al., 2014), and network-level properties such as upstream inputs (Buzsáki, 2002). By providing a window into both the single-cell properties and the integration of synaptic inputs into firing output, single-cell membrane potential recordings *in vivo* in awake animals are essential to our understanding of the relationship between neuronal computation and brain states.

The hippocampus integrates multimodal information and plays a critical role in the encoding, consolidation and retrieval of episodic memories (Buzsáki and Moser, 2013; Eichenbaum, 2016). In the hippocampus, different brain states are associated with distinct sensory integration properties as well as specific memory functions. Oscillatory dynamics and the firing patterns of neural ensembles in the hippocampus support spatial coding as demonstrated by a large number of studies based on extracellular recordings in freely behaving animals (Buzsáki and Moser, 2013). During wakefulness, periods of locomotion are associated with robust theta (4–12 Hz) and gamma (30–80 Hz) oscillations in the LFP. Since their discovery in the rabbit hippocampus, theta rhythms have been extensively studied and found in many species including rats, mice, monkeys and humans (Ekstrom et al., 2005; Green and Arduini, 1954; Jutras et al., 2013; Vanderwolf, 1969). The percentage of time in which theta is present in the LFP can predict the rate of acquisition and the quality of a memory, suggesting an important role for theta in the formation of memories (Berry and Thompson, 1978; Gupta et al., 2012; Landfield et al., 1972; Mizuseki et al., 2009). Additionally, theta correlates with behaviors associated with active sampling of the environment, like exploring, sniffing and whisking, and therefore appears well suited for the coordination of multimodal sensory integration coming from the entorhinal cortex (Komisaruk, 1970; Macrides et al., 1982). During non-locomotor behaviors, such as immobility, eating, drinking, and grooming, as well as during slow wave sleep, large irregular activity (LIA) can be detected in the hippocampal LFP. The LIA pattern is marked by high-amplitude broadband fluctuations rather than oscillations at a specific frequency band and is often characterized by the presence of sharp-waves (40-100 ms duration) that co-occur with high-frequency ripple oscillations (80-250 Hz) (SWRs) in the CA1 LFP (Buzsáki, 1986; O'Keefe, 1976; Vanderwolf, 1969). LIA is present during periods of low arousal and is thought to

represent a state in which memory consolidation and retrieval of episodic memory is promoted (Buzsáki, 2015; Carr et al., 2011).

Intracellular activity from single CA1 pyramidal cells (PCs) in awake behaving animals has provided unprecedented insight into the relationship between network and single-cell activity and its role in behavior and cognition. The combination of intracellular and multisite extracellular recordings *in vivo* in awake rodents has allowed characterizing membrane potential dynamics to reveal synaptic mechanisms of CA1 PCs SWRs (English et al., 2014; Gan et al., 2017; Hulse et al., 2016; Maier et al., 2011) and in relation to brain state and arousal (Hulse et al., 2017). CA1 hippocampal place cells have been recorded intracellularly in both freely moving (Epsztein et al., 2011) and head-fixed (Bittner et al., 2015; Cohen et al., 2017; Harvey, et al., 2009) rodents, enabling the direct measurement and manipulation of inputs and cell-intrinsic properties during spatial exploration.

Within the hippocampus, these types of studies have been mostly restricted to CA1, and the few studies that have examined the intracellular activity of CA3 PCs *in vivo* have been performed in anesthetized rats (Atallah and Scanziani, 2009; Kowalski et al., 2016) and mice (Zucca et al., 2017). CA3, the main excitatory input to CA1, is unique in both its anatomical and functional characteristics; CA3 PCs display extensive recurrent connections, and receive strong mossy fiber input from dentate granule cells (Rebola et al., 2017). Computational theories have long proposed that CA3 rapidly stores memories through synaptic plasticity in the autoassociative network formed by its recurrent connections (Kesner and Rolls, 2015), and CA3 is indeed necessary for one-trial memory encoding (Nakazawa et al., 2003). Moreover, theory and experimental evidence support that efficient episodic memory representations require a sparsely distributed neural code, in which each memory is coded by the activity of a small proportion of hippocampal neurons (Leutgeb et al., 2007; Marr, 1971; Wixted et al., 2014). To support their various functions, CA3 PCs must dynamically adapt their intracellular properties to the ongoing behavioural and brain state of the animal. To explore the modulation of intracellular dynamics of CA3 PCs in relation to changes in brain states, we performed whole-cell patch-clamp and LFP recordings in awake head-fixed mice in combination with measurements of pupil diameter and running activity on a wheel

We find that the membrane potential of CA3 PCs show different trends during theta and LIA. During theta, most CA3 PCs display a decrease in the membrane potential which is correlated with a reduced firing rate In contrast, most transitions to LIA are accompanied by a transient depolarization and correlated increase in firing rate. Moreover, the amplitude of subthreshold

membrane potential fluctuations decreases during theta and increases during LIA. Altogether, we show that different single-cell and network-level modulations are taking place during theta and LIA, impacting firing output of CA3 pyramidal cells and we propose mechanisms underlying these changes. These different modulations could underlie the ability of CA3 PCs to perform distinct memory function during different brain states.

Results

Hippocampal CA3 LFP characterization and brain state classification

To investigate the intracellular dynamics of CA3 PCs *in vivo* across brain states, we performed simultaneous whole-cell and LFP recordings in awake head-fixed mice free to run on a wheel (Figure 1A). An LFP electrode was first positioned in the *stratum pyramidale* of CA3 before lowering the patch-clamp electrode for whole-cell recordings in the vicinity of the LFP electrode. We aimed to position the tips of the LFP and patch electrodes within 200 µm of each other; electrode positions were confirmed post-hoc by histology. Pyramidal cell identity was determined by the voltage response to current steps as well as by the presence of spontaneous or evoked burst firing (Figure 1B and 1C). To monitor the level of arousal, we measured both pupil diameter and locomotor activity on the wheel (Figures 1A and 1C). Figure 1C shows an example of a current-clamp recording from a CA3 PC aligned with the corresponding LFP recording, locomotor activity and pupil diameter. We recorded a total of 35 CA3 PCs. In some cases, the patched cell was filled with biocytin and recovered in histology, confirming the cell identity (Figure 1D), and in all cases, the patch pipette position was confirmed to have been in CA3. The basic properties of each CA3 PC recorded are shown in Tables S1 and S2.

Brain state classification was achieved offline using the spectral properties of the LFP to find epochs of theta and LIA (Figures 2A and 2B), using methods similar to those previously described (Hulse et al., 2017). Theta was detected using the ratio of power in the theta (6-9 Hz) range to power in the delta (0.5-3 Hz) range (Figure 2B). From a total of 782 theta events detected from all recordings, 56% occurred in conjunction with detected locomotor activity (run theta); the remaining 44% were categorized as rest theta. LIA was detected as peaks in the average broadband power (0.5-80 Hz) after z-scoring within frequency bands; since increases in theta power alone were sometimes large enough to trigger a detectable increase in the broadband power, events that overlapped with detected theta events were not included (Figure 2B). Theta and LIA events were dispersed throughout the session with no apparent pattern (Figure 2C). Over a total recording time of 244 minutes, 14% of the time was classified as run

theta, 6% as rest theta, and 10% as LIA, leaving 70% unlabeled (Figure 2F). Out of the three event types, run theta occurred the most frequently and for the longest duration (Figure 2D and 2E). The pupil diameter of the mice was smaller during LIA as compared to theta (Figures 2G and S2). This is consistent with previous reports (Hulse et al., 2017), and provides an independent confirmation of the criteria used in the detection of brain states. Interestingly, the theta-delta ratio was significantly higher during run theta than rest theta (Figure 2H). For run theta events, increases in the theta-delta ratio often preceded the start of the detected run (Figure 2I), which has also been noted in previous studies (Fuhrmann et al., 2015; Green and Arduini, 1954; Vanderwolf, 1969). Thus, because we were able to detect theta and LIA events using the LFP positioned in the CA3 *stratum pyramidale*, we could then characterize the intracellular dynamics of nearby CA3 PCs in relation to these brain states.

Most CA3 PCs hyperpolarize during theta

We explored the membrane potential of CA3 PCs in relation to theta (Figure 3), a brain state during which spatial and episodic memory encoding is thought to preferentially occur. We performed our analyses on smoothed and downsampled membrane potential traces after spike removal (Figure S1A). We observed that the membrane potential decreased at the onset of a large proportion of theta events (Figure 3A). At the onset of theta, while the average trace of all events showed a hyperpolarization, individual theta events could be accompanied by hyperpolarization, depolarization, or no change (Figure 3B). To quantify this event-by-event heterogeneity, we compared windows before and after theta onset that aligned with the maximal change in the average trace (-2.5 to -0.5 seconds and 0.5 to 2.5 seconds). The magnitude of the change was defined as the maximal difference between the potentials in the two windows, and the significance was determined using a Welch's t-test. Out of the 743 theta events in which the membrane potential could be reliably recorded, 49% were associated with a significant hyperpolarization, 21% with depolarization and 30% showed no significant modulation (Figure 3C). Compared with randomly-selected times, there was a significantly higher proportion of hyperpolarizing events and significantly lower proportion of depolarizing and nonsignificant events, suggesting not only that the membrane potential tends to change at the onset of theta, but that this change tends to be a hyperpolarization. In addition, the duration of hyperpolarization was closely correlated with the duration of the theta event (Figure S3A). We observed no difference in the magnitude or proportion of modulation between run theta and rest theta, suggesting that the relationship between theta and membrane potential does not depend on the running behavior, but is more closely related to the internal brain state (Figure 3D). While many

cells consistently hyperpolarized during theta events, some consistently depolarized, and several cells sometimes displayed a mixed behavior of both depolarizations and hyperpolarizations. To identify the cells that either consistently hyperpolarized or consistently depolarized, we created shuffled data sets by advancing the time of the theta events with respect to the membrane potential trace; cells that showed a larger positive or negative average change than was observed in the 95% of the shuffled data were considered significantly depolarizing or hyperpolarizing, respectively. By this measure, 17 cells were significantly hyperpolarizing during theta, 2 were significantly depolarizing, and 16 showed no difference with the shuffled data set, perhaps due to a variable change in membrane potential at the onset of theta events (Figure 3E). We did not find any consistent difference in intrinsic properties between the 2 theta-depolarizing cells and the rest of the population (Tables S1 and S2).

LIA is associated with depolarization of CA3 PCs

We similarly analyzed the intracellular properties of CA3 PCs during LIA (Figure 4A). During LIA events, the membrane potential of CA3 PCs tended to depolarize, suggesting that they entered a more excitable state (Figure 4B). The depolarization tended to start before the onset of LIA and end after a few seconds, regardless of the length of the LIA state (Figure S3B). As with theta events, the membrane potential modulation was heterogeneous, with some LIA events coinciding with a depolarization, hyperpolarization, or no change (Figure 4B). Out of 403 LIA events, 44% were associated with a depolarization, 19% with a hyperpolarization, and 37% with no change, which represents more depolarizations and fewer hyperpolarizations than would be expected by chance (Figure 4C). However, when comparing each cell's modulations with those from shifted time series, only 9 cells consistently depolarized, and 25 cells showed no consistent modulation (in one cell, no LIA events were recorded) (Figure 4D). Although LIA events are associated with a high proportion of depolarizations, it seems that those depolarizations happen throughout the cell population and not specifically in a subset of cells. Therefore, many cells have a variety of responses to different LIA events, in line with recent research showing different ensembles are active during different SWRs (Ramirez-Villegas et al., 2015; Taxidis et al., 2015). Of the 9 LIA-depolarizing cells, 6 were also theta-hyperpolarizing, suggesting that this is a common combination of responses and that there is considerable overlap between cells that are consistently modulated by either brain state (Figure 4E, Table S1). We also examined whether the cells active during theta consistently reactivated during LIA, but we did not find evidence for this in our small population of theta-depolarizing cells (Table S1).

Changes in firing rate correlate with state-associated changes in membrane potential

We then asked if the observed modulation of membrane potential of CA3 PCs during theta and LIA have an impact on their firing properties. Indeed, significant changes in membrane potential for either brain state had a corresponding change in average firing rate, both in individual events and in cell averages (Figure 5A and 5B). Analysis of the inter-spike intervals (isi) revealed that, as expected, the CA3 cells had a high proportion of spikes with short isi, but that this distribution did not differ between states (Figure S4A). A characteristic property of hippocampal PCs is the propensity to fire in bursts known as complex spikes (CS), which are thought to play a role in coding and plasticity (Csicsvari et al., 1998; Magee and Johnston, 1997). Changes in CSs, which could occur due to changes in input synchrony or synaptic integration (Harris et al., 2001), would influence downstream targets, as complex and single spikes have different impacts on spike transmission efficacy (Csicsvari et al., 1998). Comparing across states, we did not observe any meaningful differences in CS properties, including the number of spikes within the CS, the amplitude or duration of the subthreshold depolarization, the amplitude of the after-hyperpolarization, the inter-CS interval (Figure 5D), the CS rate, or the proportion of spikes occurring within CSs (CS index) (Figure 5E). Additionally, there was no clear relationship between changes in CS index and changes in membrane potential during theta or LIA (Figure S4B and S4C). Thus, the firing rate increases or decreases depending on the state-dependent membrane potential modulation of a cell, however there is no specific change in CSs frequency or properties associated with changes in brain states.

Spike threshold dynamics does not reveal state-dependent changes in excitability

We next asked if the state-associated changes in membrane potential led to firing rate changes by bringing the cell closer to or further from the spike threshold. The threshold was defined as the voltage at which the change in membrane potential exceeded 5 V/s. Since threshold is modulated within complex spikes, we restricted this analysis to only spikes that had a prior inter-spike interval of at least 50 ms. We found that individual cells had spike thresholds that varied by several mV over short time scales (Figure 6A). This was correlated with the baseline membrane potential taken from the 50-300 ms window before the spike, suggesting that the spike threshold adapts to slow changes in the membrane potential and counteracts the tendency of the cell to fire (Azouz and Gray, 2003; Epsztein et al., 2011). However, the distance between baseline membrane potential and threshold decreases at depolarized membrane potentials, suggesting that slow changes in membrane potential have some ability to bring the cell closer to spike threshold (Figure 6B). The relative threshold, measured as the difference between the spike threshold and the membrane potential during the 50-300 ms prior to the spike, did not

consistently change between the states (Figure 6C), suggesting that the state-dependent changes in membrane potential were insufficient to bring the cell closer to or further from spike threshold. Next, we looked at the pre-spike depolarization (PSD), defined as the difference in voltage between the spike threshold and the membrane potential 20 ms prior to the spike (Poulet and Petersen, 2008). The PSD gives a measure of the amount of coincident input necessary to elicit a spike. We did not find any state-dependent changes (Figure 6D), suggesting that changes in firing were not due to changes in excitability; the same amplitude of rapid depolarization was necessary to elicit spikes in each state. These results suggest that absolute threshold varies dynamically for a given cell, and that the distance between ongoing membrane potential and absolute threshold stays similar across brain states. Thus, LIA-depolarizing cells do not increase their firing rate due to a change in excitability, but rather, an increase in the frequency or amplitude of synaptic inputs.

State-associated changes in membrane potential and firing rate correlate with changes in ion channel activity and synaptic input

To provide a mechanistic explanation for the modulation of membrane potential observed during theta and LIA, we examined the correlation between the change in membrane potential and the initial membrane potential before the state transition (Figure 7A). To exclude the possible influence of the holding current imposed on the cell membrane, we restricted this analysis to recording times with less than an absolute value of 10 pA holding current injected through the patch pipette. The initial membrane potential correlated with the amplitude and direction of the change in membrane potential during theta events. Specifically, larger hyperpolarizations occurred at more depolarized initial membrane potential (Figure 7B). In contrast, during LIA, the change in membrane potential does not appear to be influenced by the initial membrane potential value (Figure 7C).

To further test whether the membrane potential changes were due to modulations in ion channel activity, we measured the input resistance in a separate set of 13 cells during theta and LIA (Figure 7D). Dynamic changes in input resistance could reflect opening or closing of ion channels and result in changes in synaptic integration. During theta, input resistance significantly decreased in 6 out of 13 cells (Figure 7E). In contrast, during LIA, 6 cells out of 13 increased their input resistance (Figure 7F). Although not present in every cell, a decrease in input resistance during theta could be the result of shunting inhibition, which would be consistent with membrane potential hyperpolarization as we report here. In contrast, an increase in input

resistance during LIA could lead to an increase in synaptic integration at the soma, consistent with membrane potential depolarization and increased firing rate.

As a proxy for changes in synaptic activity, we analyzed the synaptic noise by measuring the variance of the membrane potential during LIA and theta (Figure 8). Synaptic noise refers to the irregular membrane potential fluctuations of neurons *in vivo,* which are caused by synaptic events reflecting the discharge of presynaptic neurons. Figure 6A shows an example of the membrane potential of a cell after spike removal (top black trace) and smoothing (grey trace). The residual trace was calculated by taking the difference between the spike-removed and smoothed traces; the variance was measured from this trace in sliding windows of 1 second. In comparison to all other times, the variance was significantly lower during theta and significantly higher during LIA (Figure 8B). This relationship does not seem to depend on whether the cells hyperpolarize or depolarize; that is, theta-depolarizing cells also have reduced variance during theta, and LIA-hyperpolarizing cells have increased variance during LIA. This is important to note because the variance tends to be correlated with the average membrane potential. This led us to ask whether the brain state can influence the variance beyond the effects expected from a change in membrane potential. To do this analysis, we first identified all the significant hyperpolarizing and depolarizing events and separated them based on whether they coincided with the onset of theta or LIA. The average traces of membrane potential and variance for all hyperpolarizations and depolarizations are shown in Figures 8C and 8D, respectively. The variance was then taken at the end of each hyperpolarization or depolarization. Variance was lower during theta-associated than LIA-associated hyperpolarizations (Figure 8C), and the same was true of depolarizations (Figure 8D). Taken together, these results suggest that the reduction in variance that occurs during theta is not merely a byproduct of the change in membrane potential and that a specific mechanism is taking place to reduce variance during theta. Similarly, LIA is accompanied with a greater increase in variance than what would normally occur with a depolarization. Increased synaptic input from GABAergic interneurons should normally favor hyperpolarization, with an initial increase in synaptic noise followed by a decrease as the cell membrane approaches the reversal potential for chloride. Consistent with this hypothesis, we found a nonzero delay between hyperpolarization of the membrane potential and changes in variance, but this was not state-dependent (Figure S5).

Discussion

Modulations in single-cell properties, such as resting membrane potential, intrinsic excitability and synaptic activity are thought to underlie the ability of brain circuits to generate the activity patterns that correlate with distinct brain states (Marder et al., 2014). In the neocortex, recordings of single cell membrane potential dynamics across brain states and during behavior have been key in elucidating the cellular mechanisms underlying the occurrence of distinct network activity patterns (Crochet and Petersen, 2006; Polack et al., 2013; Schneider et al., 2014). In the hippocampus of awake behaving rodents, modulation of the activity of neural ensembles and network oscillations has been extensively studied, especially regarding spatial information processing (Buzsáki and Moser, 2013). Here we have examined the intracellular dynamics of CA3 PCs in awake mice and we propose mechanisms that underlie firing rate changes CA3 during different brain states.

During theta, hippocampal pyramidal cells are engaged in encoding and recall of information. In a given environment, a proportion of CA3 PCs will be active while the majority are silent (Leutgeb, 2004). In our intracellular recordings, most of the cells hyperpolarized and, when firing, had a decreased firing rate, consistent with the findings made with extracellular recording techniques (Leutgeb, 2004). These results did not depend on whether the theta event overlapped with detected running, suggesting that hyperpolarization of CA3 PCs relate to the state of the hippocampal network rather than to the behavior of the animal. Moreover, the duration of the hyperpolarizations closely matched the total duration of the theta events, suggesting a tight temporal coupling between the underlying mechanism and theta. Interestingly, 2 of the 35 recorded CA3 PCs consistently depolarized during theta. These cells may represent a specific CA3 PC population, based on morphology (e.g. athorny CA3 PCs, Hunt et al, 2018) or coding properties, an interesting area for further study.

During theta, we observed a decrease in the variance of the membrane potential fluctuations in CA3 PCs (synaptic noise) regardless of the change in membrane potential, a slight decrease in cell input resistance, and a dependence on the initial membrane potential value, all of which point to a global increase in inhibition. However, we cannot pinpoint whether this apparent increase in inhibition is due to neuromodulation (Polack et al., 2013) or synaptic inhibitory inputs, nor can we definitively exclude other mechanisms for hyperpolarization, such as a decrease in excitatory input. It remains intriguing that a few cells show consistent activation during theta, despite the so-proposed background of global inhibition. Nevertheless, we have observed a robust phenomenon in intracellular dynamics that selects a few cells and excludes others from

the ensemble of active neurons, thus ensuring a high signal-to-noise ratio in the population firing.

In contrast to our results, it has been reported that CA1 PCs recorded in similar conditions display no marked modulation of membrane potential during theta (Hulse et al., 2017). However, optical recording of CA1 PCs using voltage sensitive dyes shows a decrease in firing rate and in the power of subthreshold fluctuations during walking, a behavior associated with theta oscillations in the hippocampus (Adam et al., 2019). This modulation of CA1 PCs occurs together with increased activity of SST interneurons, possibly driven by the medial septum (Adam et al., 2019). It is possible that a similar mechanism is taking place in the CA3 network during theta and contributes to the modulations we report.

During LIA, the brain is in a low-arousal state and hippocampal pyramidal cells engage in offline replay of sequences associated with previously learned information. A detailed analysis of membrane potential fluctuations in CA1 PCs and in DG cells across transitions to LIA was recently made in awake head-fixed mice (Hulse et al., 2017). Most cells in both CA1 and DG depolarized and their membrane potential demonstrated increased variance. We observed similar features for CA3 PCs, although to a lesser extent. Thus, during LIA, the intracellular properties of the principal hippocampal subtypes are biased toward excitation and transfer of information along the hippocampal trisynaptic pathway, possibly linked to a propensity to generate and transfer SWRs which are important for memory consolidation (Buzsáki, 2015; Foster and Wilson, 2006). While the population of CA3 PCs tended to depolarize, most cells did not do so consistently; instead they displayed different membrane potential modulation (hyperpolarization, depolarization or no change) across LIA events. We hypothesize that individual cells are activated during some LIA events but not others, which fits well with previous research showing that different SWRs activate specific ensembles (Ramirez-Villegas et al., 2015; Taxidis et al., 2015). The increased membrane potential variance in CA3 PCs and known depolarization in upstream DG suggests that CA3 PCs experience an increase in excitatory input during LIA, leading to an increase in firing rate even if the cells' excitability is stable across brain states.

In neocortical neurons, membrane potential and variance are proposed to exhibit a U-shaped dependence on arousal; compared with low-arousal states, cells are hyperpolarized during intermediate arousal, and depolarized during phasic or tonic periods of hyper-arousal, which include periods of locomotion (McGinley et al., 2015). A similar relationship in CA1 PCs was recently proposed (Hulse et al., 2017). To determine whether CA3 PCs follow the same pattern,

we would need to detect small irregular activity (SIA) (Jarosiewicz and Skaggs, 2004), which is a brain state of intermediate arousal marked by a decrease in total power in the CA1 LFP during immobility (Whishaw and Vanderwolf, 1971). During SIA, pyramidal cells in CA1 and CA2, but not CA3, code for position despite the absence of locomotion (Jarosiewicz et al., 2002; Kay et al., 2016). This may suggest that SIA in CA3 could have a specific impact on the activity of single CA3 PCs. However, we were not able to confidently detect SIA events in our data, likely due to a need to optimize recording and detection of this brain state specifically in CA3. Analysis of intracellular properties of CA3 PCs during SIA and other brain states is an interesting area for future study.

In this study, we show that transitions across brain states are reflected by coordinated changes in subthreshold intracellular dynamics of CA3 PCs. We propose that while theta and LIA induce different changes in cellular and network properties, these are balanced to ensure that only selected cells participate in the active neuronal ensemble. During theta, a small subpopulation of CA3 PCs is selectively activated by depolarization while most CA3 PCs are silenced by hyperpolarization, ensuring a high signal-to-noise ratio. In contrast, during LIA, an increase in excitatory synaptic input leads to an increase in firing rate even if cell excitability stays constant. These data demonstrate that within a cell population, intracellular properties adapt to changes in brain state to maintain sparse firing in the network.

Experimental procedures

All experiments were approved by the Ethical Committee #50 and the French Ministry for Education and Research.

Animals

C57Bl6/j male mice were obtained from Charles River and cared for according to the regulations of the University of Bordeaux/CNRS Animal Care and Use Committee. Animals were housed with their littermates with *ad libitum* access to food and water. Cages were kept in a temperature-regulated room on a 12 h light/dark cycle. Electrophysiological recordings were performed on P45-to-P71 mice.

Surgery

Headbar implantation

Custom-made stainless steel head bars (35x3x3 mm) were affixed to the skulls of 4-to-5-week-old mice using Superbond (Phymep) and dental acrylic (Dentalon, Phymep) while under isoflurane anesthesia. The skull underneath the head implant opening was covered with superbond and future locations for the craniotomies above CA3 were marked using stereotactic coordinates (2.0 caudal, 2.0 lateral from bregma).

Craniotomy

The day of recording, animals were anesthetized using isoflurane and a craniotomy (~1.5 mm diameter) was drilled at previously marked location. The dura was left intact and craniotomy was covered with silicone elastomer (Kwik-cast, World Precision Instruments). Mice were placed in a recovery cage for at least 1.5 hours before recording. Mice were typically recorded over two consecutive days.

Training

After headbar implantation, mice were left 2-3 days for recovery, until they started to gain weight again. On the first day of training, mice were allowed to freely explore the wheel for 15 min without being headfixed. During the following 4 days, mice were progressively headfixed (10 min, 30 min, 60 min, and 120 min). Thereafter, mice were headfixed 120 min each day until they habituated and were alternating between running and stopping without showing signs of excessive stress (freezing, escape attempts, struggling, excessive excretion, vocalization). Typically, mice habituated in 2 to 10 days. During the final two days of training, mice were headfixed on the principal wheel used for the recordings and habituated to the ambient light and noises that would occur during an experiment.

Recordings

Whole-cell recordings

Before attempting whole-cell patching, the depth of the pyramidal cell layer was detected using an extracellular electrode. Extracellular electrodes were glass patch electrodes (World Precision Instruments) prepared with a vertical puller PC-10 (Narishige) and then broken so that the resistance when filled with standard Ringer's solution (in mM: 135 NaCl, 5.4 KCl, 5 HEPES, 1.8 CaCl2, and 1 MgCl2) was 0.8–1.5 MΩ. The extracellular electrode used to determine the pyramidal cell depth for whole-cell recording was mounted vertically on a micromanipulator (Scientifica). As the electrode was advanced through the cortex, the CA1 pyramidal cell layer was identified when multi-unit activity could be detected and the amplitude of ripples increased, typically 1.3–1.5 mm below the surface of the brain. The polarity of the sharp waves inversed below the CA1 pyramidal layer, and the electrode was advanced further down the hippocampus until the sharp waves changed polarity again (to positive) and multi-unit activity was detected, indicative of the CA3 pyramidal layer. The extracellular electrode to be used for LFP recordings during whole-cell patching was mounted on a second micromanipulator (Luigs and Neumann) at a 22.5° angle relative to the vertical axis, and advanced through the same craniotomy at a more medial and caudal position. This extracellular electrode was advanced until detection of the pyramidal cell layer but not through it. The two LFPs were recorded for visual confirmation of a high correlation between the two signals (phase of theta, coincidence of ripples, multi-unit activity), indicative of a short distance between the two recording sites. Whole-cell patch electrodes (3.5-5 MΩ) were prepared beforehand and were filled with a solution containing (in mM) 134 K-methanesulfonate, 2 KCl, 10 HEPES, 10 EGTA, 2 MgCl2, and 2 Na-ATP, at 290–300 mOsm and pH 7.2–7.3 adjusted with KOH. The intracellular solution was supplemented with 0.2% (w/v) biocytin for post hoc cellular identification and morphological reconstruction. Whole-cell patch-clamp recordings were achieved using a standard blind-patch approach as previously described (Lee et al., 2009; Margrie et al., 2002). Access resistance and membrane capacitance of the cells were monitored on-line with the membrane test feature of the acquisition software and analyzed off-line. The mean access resistance was 52.4 ± 2.5 MΩ. Membrane potential was not corrected for liquid junction potential which was estimated to be approximatively 11 mV (LJP calculator, Clampex). Recordings were discarded when the access resistance exceeded 100 MΩ or when the action potential peak dropped below 0 mV.

Data acquisition

Electrophysiology

All recordings were made in the current-clamp configuration. Recordings were obtained with a Multiclamp 700B amplifier connected to the Digidata 1440A system. Data were acquired with pClamp 10 (Molecular Devices), digitized at 10 kHz, filtered at 3 kHz, and analyzed off-line with Clampfit 10.4 (Molecular Devices) and Python. To measure input resistance, we injected trains of current pulses (-100 pA, 100 ms) in a separate set of recordings (n = 13).

Pupil recording

Pupil diameter was measured for a subset of recordings (n=11/35). To measure pupil diameter, the mouse was illuminated with an infrared (850 nm) battery-operated light (Maketheone IR Torch 850NM) and imaged with a camera (DALSA GENIE NANO-M1280-NIR) at 10 Hz.

Locomotion

Online running behavior and the animal's velocity during the recording session was measured using Poly Wheel software (Imetronic, France) and acquired at 32 Hz. Locomotion was detected as IR-sensor-crossing by the animal. 16 sensors were located on a wheel of 20 cm diameter.

Histology

To recover the morphology of neurons filled with biocytin during *in vivo* whole-cell patch-clamp recordings, brains were removed after the completion of electrophysiology experiments and were fixed for 1 week at 4°C in a solution containing 4% PFA in 1X PBS, pH7.4. Coronal slices (100 µm thick) were incubated overnight at 4°C in 1:1000 Alexa Fluor 488 conjugated in the same solution. Images were acquired using a confocal microscope (TCS SP8, Leica) and oil objective HC PL APO 40x/1.30.

Analysis

LFP

LFP signal was downsampled 10 times to 2000 Hz and filtered using a 4-pole butterworth band-pass filter between 0.2 Hz and 100 Hz. After filtering, LFP was again downsampled to 200 Hz. The spectrogram of the LFP was calculated using consecutive fast Fourier transforms within ~2 second boxcar windows with 99% overlap. Theta/delta ratio was found by dividing the average power in the theta range (6-9 Hz) by the average power in the delta range (0.5-3.5 Hz). This ratio was normalized within sessions by taking the z-score. For the total power, the spectrogram was z-scored within frequency bands, and averaged between 0.3 and 80 Hz.

Brain state classification

Theta events were identified as periods with a theta/delta power ratio above the mean. To be counted as theta events, theta bouts had to be longer than 1 s and have a power ratio higher than 1 sd above the mean at least once. If two theta bouts happened less than 1 s apart, they were merged into one single theta period. LIA events were identified as periods with a total LFP power above the mean. To be counted as LIA events, LIA bouts had to be longer than 2 s and have a total power higher than 0.25 sd above the mean at least once. If two LIA bouts happened less than 0.5 s apart, they were merged into one single LIA period.

Membrane potential

Analysis of membrane potential changes was performed on membrane potential traces after spike removal. Spikes were detected when the derivative of the membrane potential (dV/dt) exceeded 5 mV/ms. To keep a conservative estimate of average membrane potential, spikes and their underlying depolarizations such as plateau potentials were removed (Figure S1). The spike-removed membrane potential trace was then smoothed by taking the mean over a sliding window of 2 s, and the smoothed membrane potential was downsampled to 20 Hz. The residual membrane potential trace was obtained by subtracting the smoothed membrane potential from the spike-removed membrane potential. From this residual membrane potential, the variance was calculated over a sliding a window of 1 s. The variance trace was then smoothed by taking the mean over a sliding window of 2 s and downsampled to 20 Hz.

Input resistance

Input resistance was calculated using the voltage response to 100 ms steps of -100 pA current. The average voltage during the 250 ms before the current pulse was subtracted from the 250 ms before the end of the current pulse, and the result was divided by the amplitude of the current pulse. Input resistance measurements were discarded when spikes were detected occurring in a window of 750 ms centered around either sample period.

Detection of complex spikes

The time stamp and threshold potential for each spike was taken as the time and membrane potential when the first derivative (dV/dt) first surpassed 5 V/s. The end of each spike was detected as the first local minimum after the peak of the spike. A subthreshold potential trace was created by removing the spikes and linearly interpolating between the start and end of the spikes. This method preserved the subthreshold depolarizations characteristic of complex spikes. Complex spike initiation was detected as any group of three or more spikes that had an isi of 20 ms or less. The start time and voltage of the complex spike was defined as that of the threshold of the first spike in the burst. The end of the complex spike was defined as the first

local minimum after the subthreshold potential returned to within 3 mV of the starting voltage of the complex spike. Any spikes that occurred between the start and the end of the subthreshold component of the complex spike were considered part of that complex spike, regardless of their inter-spike interval.

Spike threshold

The time stamp and threshold potential for each spike was taken as the time and membrane potential when the first derivative (dV/dt) first surpassed 5 V/s. To restrict the analysis to spikes that were either isolated or the first in a complex spike, spikes that had a prior inter-spike interval of less than 50 ms were eliminated from the analysis. In addition, spikes that were in a CS, but not the first spike, were also eliminated. Spikelets were also eliminated by discarding spikes that occurred outside of CS and did not reach peak amplitude of at least -10 mV. The distance to spike threshold for each spike was calculated by subtracting the spike threshold from the baseline membrane potential over a specified period prior to the spike. The baseline membrane potential was defined as the mode of the voltages after spike removal (replacing spikes and their subthreshold components with nans instead of linearly-interpolated values), smoothing over windows of 2ms, downsampling to 500 Hz, and rounding all values to the nearest 0.1 mV.

Pupil diameter

To measure pupil diameter, frames were extracted from the video file. A Circle Hough Transform (CHT) was performed to detect circular objects in each individual frames. The radius of the detected circles was extracted automatically. Pupil diameter data was included after control of correct pupil detection. The resulting pupil diameter trace was smoothed with a 4-pole butterworth low-pass filter (0.5 Hz cutoff).

Statistics

Unless otherwise noted, data were expressed as the median +/- the mean absolute derivation about the median, which was calculated by subtracting each data point from the group's median, taking the absolute value, summating, and then dividing by the number of data points. These measures of central tendency and variation were used because many distributions were found not to be normal. When comparing 2 independent groups, a bootstrapping method was used. Briefly, data from both groups were randomly resampled with replacement to form two surrogate groups. This was repeated 1,000 times, and if the difference in medians was more extreme than 95% of the surrogate trials, the groups were considered significantly different. For comparisons of 3 or more groups, a Kruskal-Wallis test was performed to determine the presence of any significantly different group before performing the 2-group bootstrap for each group pair. A

different bootstrap test was used when comparing two non-independent groups. In this test, the difference between paired data points was randomly determined to be either positive or negative 1,000 times. If the mean of the differences in the actual data set was more extreme than 95% of those in the shuffled data set, the paired groups were considered to have a significant difference. For comparative scatter plots where variables during different states were compared, a Mann-Whitney U test was used to determine whether there was a significant difference between the states for that particular cell (filled circles in scatter plots). When determining whether a value was significantly different from zero, a bootstrapping method was used. The distribution was demeaned and then resampled with replacement 10,000 times. If the mean of the original data was more extreme than 95% of the resampled means, it was considered significantly different from zero.

To determine whether a particular event was associated with a significant change in membrane potential, 2 two-second windows of the 20 Hz downsampled membrane potential around the start of the event were compared with a Welch's t-test. For theta, the comparison was made between –2.5 to –0.5 and 0.5 to 2.5 seconds with respect to the start of the event; for LIA, the windows were –4 to –2 and –1 to 1 second. Events with p-values less than 0.05 were considered to be hyper- or depolarizing depending on the direction of the change in membrane potential. To determine whether the proportions of hyperpolarizing, depolarizing and no change events could be due to chance, a bootstrapping method was used. For every recording, the actual event times were replaced with randomly-sampled times, and the same method as previously described was used to determine whether each random timepoint was associated with a hyperpolarization, depolarization, or no change. This was repeated 1,000 times to create a distribution of proportions. Proportions were considered significantly different from chance if they were either greater or smaller than 95% of the randomly-sampled data sets.

To determine whether a cell was consistently changed membrane potential at the start of a particular type of event, we used a bootstrapping method. Over a single recording session, the membrane potential and actual event times were shifted in time with respect to one another 6,000 times in increments of 50 ms. For each shift, the average change in membrane potential associated with event onset was calculated for the cell. Cells were considered significantly hyper- or depolarizing when the average change in membrane potential was more extreme than 95% of the shuffled data.

Ackowledgements

This study was supported by the Centre National de la Recherche Scientifique, the European Commission (EIF Fellowship awarded to AK), the ANR (grant Hippencode), and the Fondation pour la Recherche Médicale (to MM). We are grateful to Ania Gonçalves for help in confocal imaging and Mario Carta, Lisa Roux and Xavier Leinekugel for useful comments on the manuscript and fruitful discussions.

References

Adam, Y., Kim, J.J., Lou, S., Zhao, Y., Xie, M.E., Brinks, D., Wu, H., Mostajo-Radji, M.A., Kheifets, S., Parot, V., et al. (2019). Voltage imaging and optogenetics reveal behaviour-dependent changes in hippocampal dynamics. Nature.

Atallah, B. V, and Scanziani, M. (2009). Instantaneous modulation of gamma oscillation frequency by balancing excitation with inhibition. Neuron *62*, 566–577.

Azouz, R., and Gray, C.M. (2003). Adaptive coincidence detection and dynamic gain control in visual cortical neurons in vivo. Neuron *37*, 513–523.

Berry, S.D., and Thompson, R.F. (1978). Prediction of learning rate from the hippocampal electroencephalogram. Science *200*, 1298–1300.

Bittner, K.C., Grienberger, C., Vaidya, S.P., Milstein, A.D., Macklin, J.J., Suh, J., Tonegawa, S., and Magee, J.C. (2015). Conjunctive input processing drives feature selectivity in hippocampal CA1 neurons. Nat. Neurosci. *18*, 1133–1142.

Buzsáki, G. (1986). Hippocampal sharp waves: their origin and significance. Brain Res. *398*, 242–252.

Buzsáki, G. (2002). Theta oscillations in the hippocampus. Neuron *33*, 325–340.

Buzsáki, G. (2015). Hippocampal sharp wave-ripple: A cognitive biomarker for episodic memory and planning. Hippocampus *25*, 1073–1188.

Buzsáki, G., and Moser, E.I. (2013). Memory, navigation and theta rhythm in the hippocampal-entorhinal system. Nat. Neurosci. *16*, 130–138.

Carr, M.F., Jadhav, S.P., and Frank, L.M. (2011). Hippocampal replay in the awake state: A potential substrate for memory consolidation and retrieval. Nat. Neurosci. *14*, 147–153.

Cohen, M.X. (2017). Where Does EEG Come From and What Does It Mean? Trends Neurosci. *40*, 208–218.

Crochet, S., and Petersen, C.C.H. (2006). Correlating whisker behavior with membrane potential in barrel cortex of awake mice. Nat. Neurosci. *9*, 608–610.

Csicsvari, J., Hirase, H., Czurko, A., and Buzsáki, G. (1998). Reliability and state dependence of pyramidal cell-interneuron synapses in the hippocampus: An ensemble approach in the behaving rat. Neuron *21*, 179–189.

Eichenbaum, H. (2016). Still searching for the engram. Learn. Behav. *44*, 209–222.

Ekstrom, A.D., Caplan, J.B., Ho, E., Shattuck, K., Fried, I., and Kahana, M.J. (2005). Human hippocampal theta activity during virtual navigation. Hippocampus *15*, 881–889.

English, D.F., Peyrache, A., Stark, E., Roux, L., Vallentin, D., Long, M.A., Buzsaki, G., and Buzsáki, G. (2014). Excitation and Inhibition Compete to Control Spiking during Hippocampal Ripples: Intracellular Study in Behaving Mice. J Neurosci *34*, 16509–16517.

Epsztein, J., Brecht, M., and Lee, A.K. (2011). Intracellular Determinants of Hippocampal CA1 Place and Silent Cell Activity in a Novel Environment. Neuron *70*, 109–120.

Foster, D.J., and Wilson, M.A. (2006). Reverse replay of behavioural sequences in hippocampal place cells during the awake state. Nature *440*, 680–683.

Fuhrmann, F., Justus, D., Sosulina, L., Kaneko, H., Beutel, T., Friedrichs, D., Schoch, S., Schwarz, M.K., Fuhrmann, M., and Remy, S. (2015). Locomotion, Theta Oscillations, and the Speed-Correlated Firing of Hippocampal Neurons Are Controlled by a Medial Septal Glutamatergic Circuit. Neuron *86*, 1253–1264.

Gan, J., Weng, S., Pernía-Andrade, A.J., Csicsvari, J., and Jonas, P. (2017). Phase-Locked Inhibition, but Not Excitation, Underlies Hippocampal Ripple Oscillations in Awake Mice In Vivo. Neuron *93*, 1–7.

GREEN, J.D., and ARDUINI, A.A. (1954). Hippocampal electrical activity in arousal. J. Neurophysiol. *17*, 533–557.

Gupta, A.S., Van Der Meer, M.A.A., Touretzky, D.S., and Redish, A.D. (2012). Segmentation of spatial experience by hippocampal theta sequences. Nat. Neurosci. *15*, 1032–1039.

Harris, K.D., Hirase, H., and Henze, D. (2001). Temporal interaction between single spikes and complex spikes bursts in hippocampal pyramidal cells. Neuron *32*, 141–149.

Harvey, C.D., Collman, F., Dombeck, D.A., and Tank, D.W. (2009). Intracellular dynamics of hippocampal place cells during virtual navigation. Nature *461*, 941–946.

Hulse, B.K., Moreaux, L.C., Lubenov, E. V, Siapas Correspondence, A.G., and Siapas, A.G. (2016). Membrane Potential Dynamics of CA1 Pyramidal Neurons during Hippocampal Ripples in Awake Mice. Neuron *89*, 800–813.

Hulse, B.K., Lubenov, E. V., and Siapas, A.G. (2017). Brain State Dependence of Hippocampal Subthreshold Activity in Awake Mice. Cell Rep. *18*, 136–147.

Jarosiewicz, B., and Skaggs, W.E. (2004). Level of Arousal During the Small Irregular Activity State in the Rat Hippocampal EEG. J. Neurophysiol. *91*, 2649–2657.

Jarosiewicz, B., McNaughton, B.L., and Skaggs, W.E. (2002). Hippocampal population activity during the small-amplitude irregular activity state in the rat. J. Neurosci. *22*, 1373–1384.

Jutras, M.J., Fries, P., and Buffalo, E.A. (2013). Oscillatory activity in the monkey hippocampus during visual exploration and memory formation. Proc. Natl. Acad. Sci. U. S. A. *110*, 13144–13149.

Kay, K., Sosa, M., Chung, J.E., Karlsson, M.P., Larkin, M.C., and Frank, L.M. (2016). A

hippocampal network for spatial coding during immobility and sleep. Nature *531*, 185–190.

Kesner, R.P., and Rolls, E.T. (2015). A computational theory of hippocampal function, and tests of the theory: New developments. Neurosci. Biobehav. Rev. *48*, 92–147.

Komisaruk, B.R. (1970). Synchrony between limbic system theta activity and rhythmical behavior in rats. J. Comp. Physiol. Psychol. *70*, 482–492.

Kowalski, J., Gan, J., Jonas, P., and Pernía-Andrade, A.J. (2016). Intrinsic membrane properties determine hippocampal differential firing pattern in vivo in anesthetized rats. Hippocampus *26*, 668–682.

Landfield, P.W., Mcgaugh, J.L., and Tusa, R.J. (1972). Theta rhythm: A temporal correlate of memory storage processes in the rat. Science (80-.). *175*, 87–89.

Lee, A.K., Epsztein, J., and Brecht, M. (2009). Head-anchored whole-cell recordings in freely moving rats. Nat. Protoc. *4*, 385–392.

Leutgeb, S. (2004). Distinct Ensemble Codes in Hippocampal Areas CA3 and CA1. Science (80-.). *305*, 1295–1298.

Leutgeb, J.K., Leutgeb, S., Moser, M.-B., and Moser, E.I. (2007). Pattern separation in the dentate gyrus and CA3 of the hippocampus. Science *315*, 961–966.

Macrides, F., Eichenbaum, H.B., and Forbes, W.B. (1982). Temporal relationship between sniffing and the limbic theta rhythm during odor discrimination reversal learning. J. Neurosci. *2*, 1705–1717.

Magee, J.C., and Johnston, D. (1997). A Synaptically Controlled, Associative Signal for Hebbian Plasticity in Hippocampal Neurons. Science (80-.). *275*, 1–5.

Maier, N., Tejero-Cantero, Á., Dorrn, A.L., Winterer, J., Beed, P.S., Morris, G., Kempter, R., Poulet, J.F.A., Leibold, C., and Schmitz, D. (2011). Coherent Phasic Excitation during Hippocampal Ripples. Neuron *72*, 137–152.

Marder, E., O'Leary, T., and Shruti, S. (2014). Neuromodulation of Circuits with Variable Parameters: Single Neurons and Small Circuits Reveal Principles of State-Dependent and Robust Neuromodulation. Annu. Rev. Neurosci. *37*, 329–346.

Margrie, T.W., Brecht, M., and Sakmann, B. (2002). In vivo, low-resistance, whole-cell recordings from neurons in the anaesthetized and awake mammalian brain. Pflugers Arch. Eur. J. Physiol. *444*, 491–498.

Marr, D. (1971). Simple Memory: A Theory for Archicortex. Philos. Trans. R. Soc. B Biol. Sci. *262*, 23–81.

McGinley, M.J., Vinck, M., Reimer, J., Batista-Brito, R., Zagha, E., Cadwell, C.R., Tolias, A.S., Cardin, J.A., and McCormick, D.A. (2015). Waking State: Rapid Variations Modulate Neural and Behavioral Responses. Neuron *87*, 1143–1161.

Mizuseki, K., Sirota, A., Pastalkova, E., and Buzsáki, G. (2009). Theta Oscillations Provide Temporal Windows for Local Circuit Computation in the Entorhinal-Hippocampal Loop. Neuron *64*, 267–280.

Nakazawa, K., Sun, L.D., Quirk, M.C., Rondi-Reig, L., Wilson, M.A., and Tonegawa, S. (2003). Hippocampal CA3 NMDA receptors are crucial for memory acquisition of one-time experience. Neuron *38*, 305–315.

O'Keefe, J. (1976). Place units in the hippocampus of the freely moving rat. Exp. Neurol. *51*, 78–109.

Polack, P.O., Friedman, J., and Golshani, P. (2013). Cellular mechanisms of brain state-dependent gain modulation in visual cortex. Nat. Neurosci. *16*, 1331–1339.

Poulet, J.F. a, and Petersen, C.C.H. (2008). Internal brain state regulates membrane potential synchrony in barrel cortex of behaving mice. Nature *454*, 881–885.

Ramirez-Villegas, J.F., Logothetis, N.K., and Besserve, M. (2015). Diversity of sharp-wave–ripple LFP signatures reveals differentiated brain-wide dynamical events. Proc. Natl. Acad. Sci. *112*, E6379–E6387.

Rebola, N., Carta, M., and Mulle, C. (2017). Operation and plasticity of hippocampal CA3 circuits: Implications for memory encoding. Nat. Rev. Neurosci. *18*, 209–221.

Schneider, D.M., Nelson, A., and Mooney, R. (2014). A synaptic and circuit basis for corollary discharge in the auditory cortex. Nature *513*, 189–194.

Taxidis, J., Anastassiou, C.A., Diba, K., and Koch, C. (2015). Local Field Potentials Encode Place Cell Ensemble Activation during Hippocampal Sharp Wave Ripples. Neuron *87*, 590–604.

Vanderwolf, C.H. (1969). Hippocampal electrical activity and voluntary movement in the rat. Electroencephalogr. Clin. Neurophysiol. *26*, 407–418.

Whishaw, I.Q., and Vanderwolf, C.H. (1971). Hippocampal EEG and behavior: effects of variation in body temperature and relation of EEG to vibrissae movement, swimming and shivering. Physiol. Behav. *6*, 391–397.

Wixted, J.T., Squire, L.R., Jang, Y., Papesh, M.H., Goldinger, S.D., Kuhn, J.R., Smith, K.A., Treiman, D.M., and Steinmetz, P.N. (2014). Sparse and distributed coding of episodic memory in neurons of the human hippocampus. Proc. Natl. Acad. Sci. *111*, 9621–9626.

Zucca, S., Griguoli, M., Malézieux, M., Grosjean, N., Carta, M., and Mulle, C. (2017). Control of Spike Transfer at Hippocampal Mossy Fiber Synapses In Vivo by GABA A and GABA B Receptor-Mediated Inhibition. J. Neurosci. *37*, 587–598.

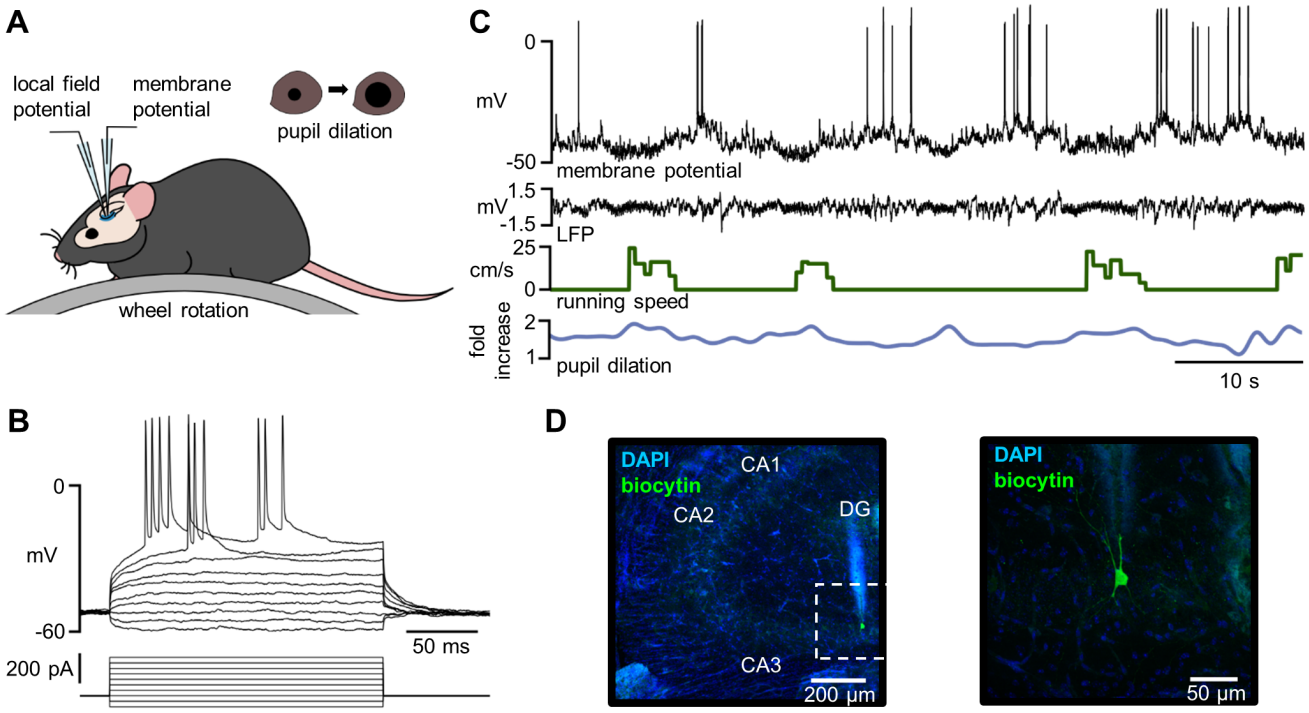
A
local field potential
membrane potential
pupil dilation
wheel rotation
C
0
mV
-50
membrane potential
1.5
mV
-1.5
LFP
25
cm/s
0
running speed
2
fold increase
1
pupil dilation
10 s
B
0
mV
-60
50 ms
200 pA
D
DAPI
biocytin
CA1
CA2
DG
CA3
200 µm
DAPI
biocytin
50 µm

Figure 1 - Experimental configuration and data recorded. (A) Schematic of the head-fixed electrophysiological recording configuration. LFP and whole-cell recordings were performed in CA3. Wheel rotation and pupil dilation of the animal were monitored during the recordings. (B) Example trace of the sub- and suprathreshold responses of a CA3 PC to injected current pulses (10 pulses, from -80 pA to 280 pA). (C) Example trace of a simultaneous current-clamp recording from a CA3 PC showing spontaneous action potentials (membrane potential, black), aligned with the nearby LFP (LFP, black) the corresponding locomotor velocity (running speed, green) and pupil diameter changes (pupil dilation, blue) of the animal. (D) Confocal fluorescent image of a 100-µm-thick coronal section of dorsal hippocampus (left; 20x) with a single CA3 PC (right; 40x) filled with biocytin during whole-cell recording and visualized by post hoc labeling with Alexa Fluor 488. Note the presence of the pipette track above the filled CA3 PC.

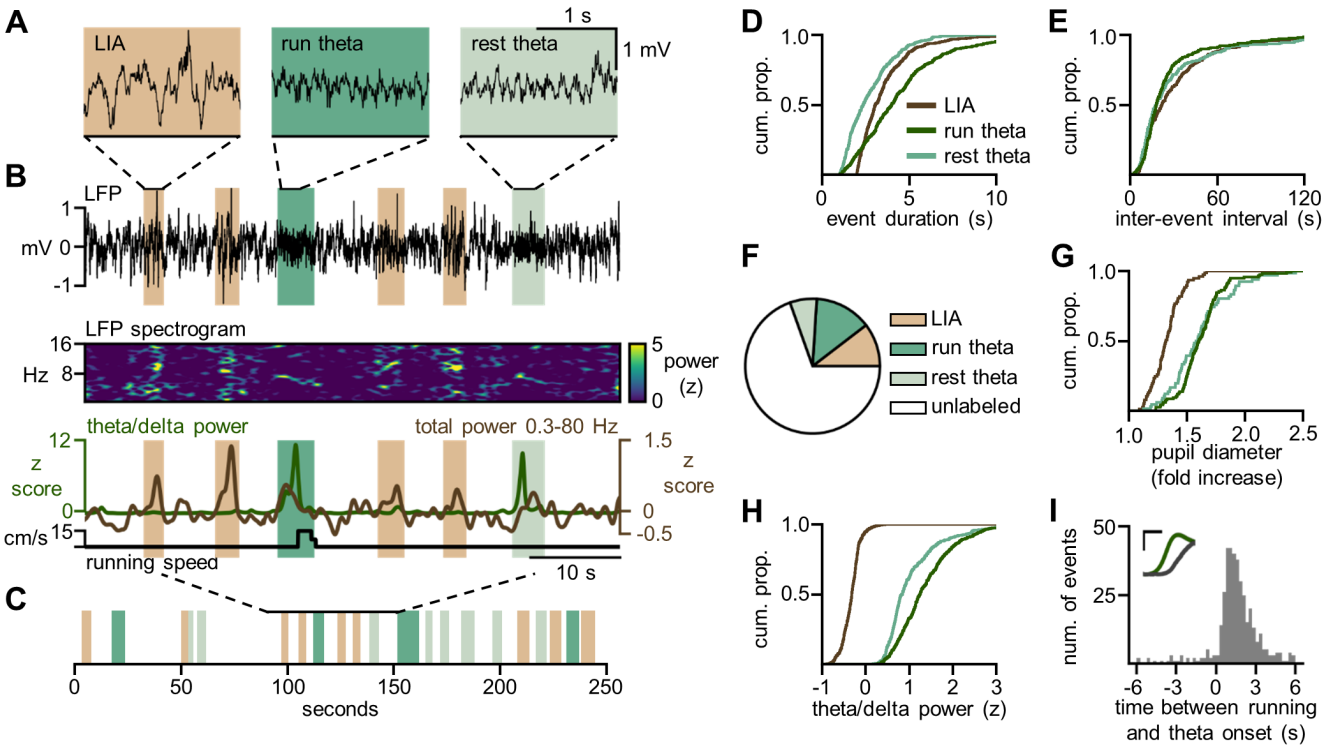
A
LIA
run theta
rest theta
1 s
1 mV
B
LFP
1
mV 0
-1
LFP spectrogram
16
Hz 8
5
power
(z)
0
theta/delta power
total power 0.3-80 Hz
12
z
score
0
1.5
z
score
0
-0.5
cm/s 15
running speed
10 s
C
0
50
100
150
200
250
seconds
D
1.0
0.5
cum. prop.
LIA
run theta
rest theta
0
5
10
event duration (s)
E
1.0
0.5
cum. prop.
0
60
120
inter-event interval (s)
F
LIA
run theta
rest theta
unlabeled
G
1.0
0.5
cum. prop.
1.0
1.5
2.0
2.5
pupil diameter
(fold increase)
H
1.0
0.5
cum. prop.
-1
0
1
2
3
theta/delta power (z)
I
50
25
num. of events
-6
-3
0
3
6
time between running
and theta onset (s)

Figure 2 - Brain state classification and characterization. (A) Example traces of LIA (brown), run theta (dark green) and rest theta (light green). Similar color scheme is used throughout. (B) Top: One minute LFP recording from CA3 with detected LIA, run theta and rest theta. Middle: Corresponding spectrogram showing z-scored LFP power between 0 and 16 Hz. Note the high broadband power present during LIA and narrow frequency band during theta events. Bottom: Theta/delta power ratio superimposed with total 0.3-80 Hz power, used in state detection. Velocity of the animal is shown below. (C) Representation of the brain states LIA, run theta and rest theta over a full recording session. (D) (E) Cumulative distribution of the duration (D) and inter-event interval (E) of the different states. Run theta events lasted longer than rest theta and LIA events (3.99 ± 1.96 s [n = 437 events] for run theta, 2.37 ± 1.11 s [n = 345 events] for rest theta, 3.06 ± 1.11 s [n = 424 events] for LIA, $p < 0.001$ for both pairs). LIA events lasted longer than rest theta ($p < 0.001$). All data are expressed in median ± average absolute deviation from the median unless otherwise stated. All event types occurred at a similar frequency (Kruskal-Wallace; $p = 0.111$). (18.66 ± 19.3 s [n = 437 events] for run theta, 19.47 ± 21.19 s [n = 345 events] for rest theta, 22.56 ± 20.19 s [n = 424 events] for LIA). (F) Total percent of time detected for each state over all the recording sessions. Over 243.6 minutes of recording there were a total of 33.1 minutes of run theta (13.6%), 15.7 minutes of rest theta (6.5%), and 25.3 minutes of LIA (10.4%). The remaining 169.4 minutes (69.5%) were left unlabeled. (G) Pupil diameter (expressed as fold increase from the minimum) during each brain state (n = 12 cells). The pupil dilated the same amount for run and rest theta ($p=0.682$), but was more dilated during both types of theta events than during LIA (1.60 ± 0.15 fold [n = 117 events] for run theta, 1.59 ± 0.20 fold [n = 66 events] for rest theta, 1.32 ± 0.10 fold [n = 77 events] for LIA, $p < 0.001$ for both pairs). (H) Theta/delta power ratio for each brain state. The z-scored theta/delta power was larger during theta than during LIA (1.26 ± 0.52 [n = 437 events] for run theta, 0.85 ± 0.46 [n = 345 events] for rest theta, -0.31 ± 0.16 [n = 424 events] for LIA, $p < 0.001$ for both pairs). This ratio was also larger during run theta compared to rest theta ($p < 0.001$). (I) Delay between the start of theta and start of running. Inset shows the average increase in theta preceding the average increase in velocity (grey) for all events (n = 435) in all cells recorded (scale bar represents 1 s, 1 unit of z-scored theta/delta ratio, 5 cm/s). Running started significantly after the start of theta (1.38 ± 5.84 s, $p < 0.001$).

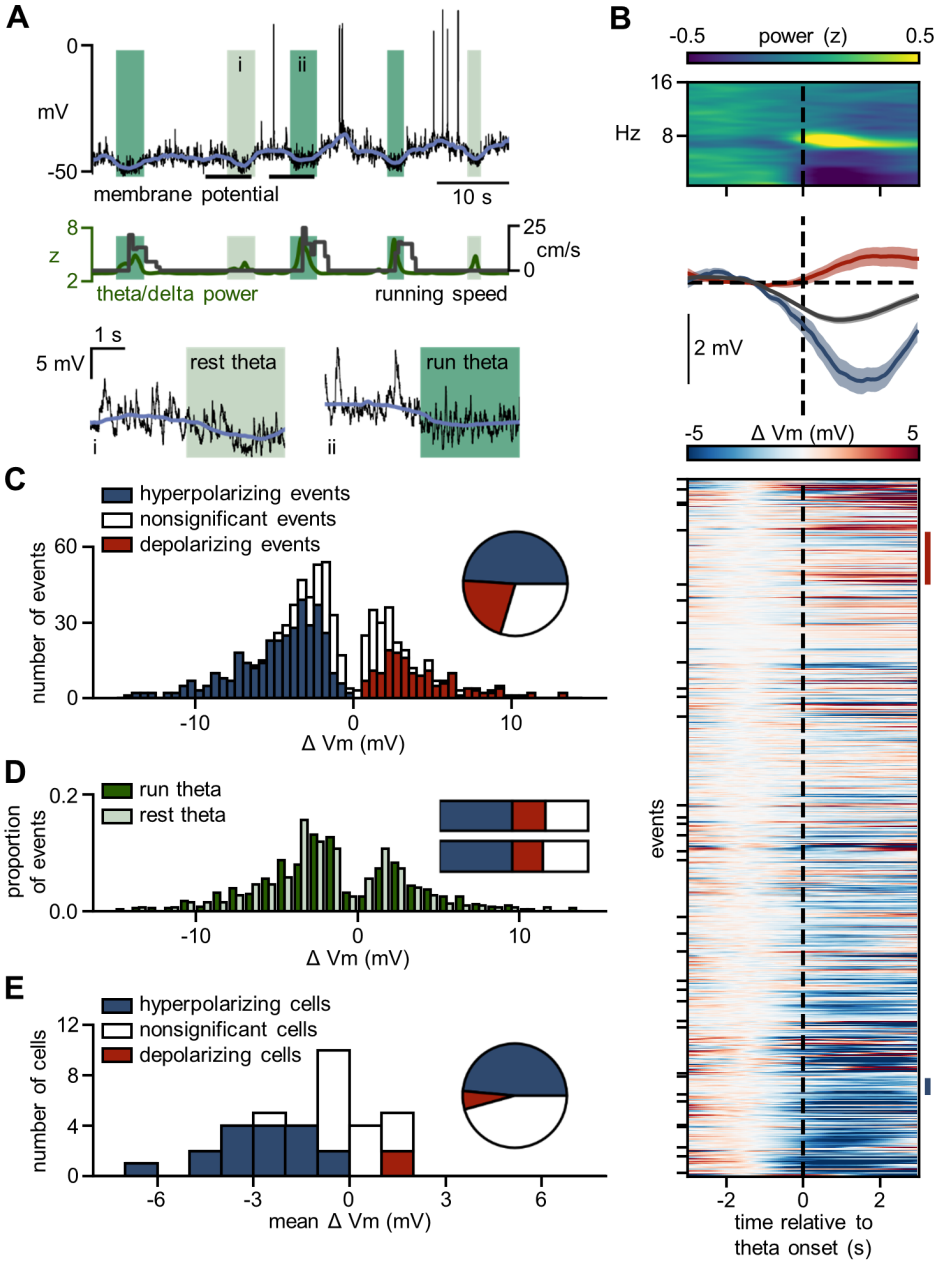
A
0
mV
-50
i
ii
membrane potential
10 s
8
z
2
theta/delta power
25
cm/s
0
running speed
1 s
5 mV
rest theta
run theta
i
ii
B
-0.5
power (z)
0.5
16
Hz
8
2 mV
-5
Δ Vm (mV)
5
events
-2
0
2
time relative to
theta onset (s)
C
hyperpolarizing events
nonsignificant events
depolarizing events
number of events
60
30
0
-10
0
10
Δ Vm (mV)
D
run theta
rest theta
proportion
of events
0.2
0.0
-10
0
10
Δ Vm (mV)
E
hyperpolarizing cells
nonsignificant cells
depolarizing cells
number of cells
12
8
4
0
-6
-3
0
3
6
mean Δ Vm (mV)

Figure 3 - CA3 pyramidal cells decrease their membrane potential during theta. (A) Example trace showing a whole-cell recording of a CA3 PC (top), with simultaneous theta/delta power ratio of the nearby LFP and the running speed of the mouse (middle). Blue trace superimposed on the raw Vm is the smoothed Vm after spike removal. Bottom: examples of Vm modulation during one rest theta and one run theta event. (B) Top: Spectrogram of the average LFP (z-scored within frequency bands) triggered by transitions to theta (time = 0, dotted line) showing an increase of power in the theta band (6-9 Hz). Middle: Average Vm traces during theta onset of an example hyperpolarizing (blue) and depolarizing (red) cell, as well as the grand average over all events (grey) (n = 743, shaded areas represent ± sem). Bottom: Color plot showing the Vm of CA3 PCs triggered by transition to theta normalized to 2.5 to 0.5 s before start of theta. Blue represents Vm hyperpolarization, red Vm depolarization. Each cell is represented in between black ticks. Cells are ordered depending on their average Vm modulation during theta, with depolarizing cells on top and hyperpolarizing cells at the bottom of the plot. Events within each cell are ordered by the time in which they occurred in the recording. Red and blue vertical lines indicate the sample cells shown in the average traces above. (C) Distribution of the magnitude of change in Vm at the onset of theta (n = 743 events, bin size = 0.5 mV). Events are colored according to whether there was a hyperpolarization (blue), depolarization (red) or no significant change (white). Similar color scheme is used throughout the figures. Inset: pie chart of the different event types (49.0% hyperpolarizing [n = 364 events], 21.4% depolarizing [n = 159 events], 29.6% no change [n = 220 events]. Compared to a shuffled data set, there were significantly more hyperpolarizing events and fewer depolarizing and nonsignificant events ($p < 0.001$ for all categories) than chance level. (D) Comparison of Vm modulation during theta for run [n = 415] and rest [n = 328] events (bin size = 1 mV). Inset: bar charts of percent event type (hyperpolarizing, depolarizing, or no change) for run (top) and rest (bottom) theta events. All types of events occurred at a similar frequency during run and rest theta ($p=0.485$ for hyperpolarizing, $p=0.624$ for depolarizing, $p=0.321$ for no change). (E) Distribution of cells' average Vm change during theta (bin size = 1 mV). Inset: pie chart of the different cell types (17 cells were hyperpolarizing, 2 cells were depolarizing and 16 cells showed no significant modulation towards one specific direction).

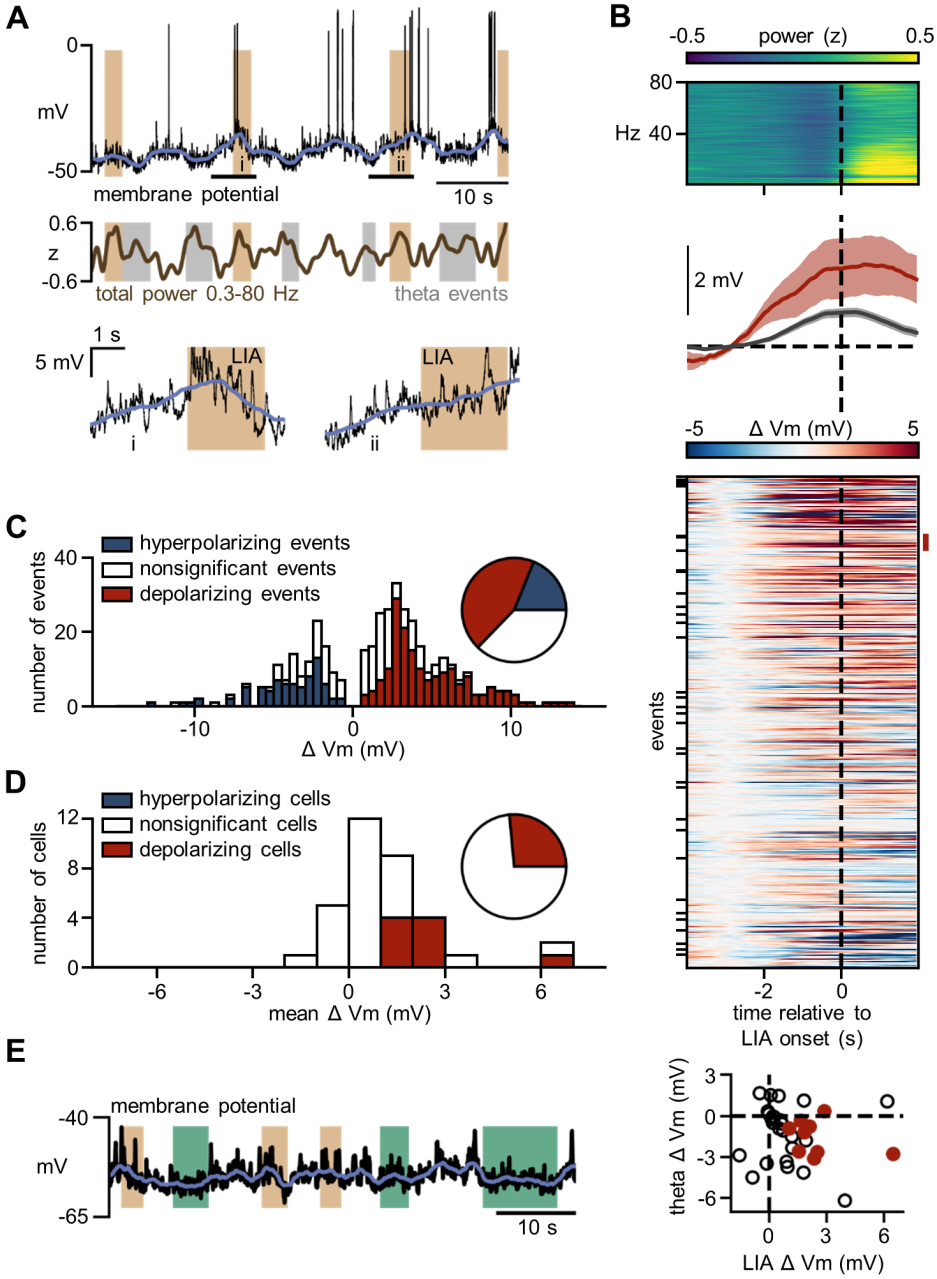
A
0
mV
-50
membrane potential
i
ii
10 s
0.6
z
-0.6
total power 0.3-80 Hz
theta events
1 s
5 mV
LIA
LIA
i
ii
B
-0.5
power (z)
0.5
80
Hz 40
2 mV
-5
Δ Vm (mV)
5
events
-2
0
time relative to
LIA onset (s)
C
hyperpolarizing events
nonsignificant events
depolarizing events
number of events
40
20
0
-10
0
10
Δ Vm (mV)
D
hyperpolarizing cells
nonsignificant cells
depolarizing cells
number of cells
12
8
4
0
-6
-3
0
3
6
mean Δ Vm (mV)
E
membrane potential
-40
mV
-65
10 s
theta Δ Vm (mV)
3
0
-3
-6
0
3
6
LIA Δ Vm (mV)

Figure 4 - CA3 pyramidal cells increase their membrane potential during LIA. (A) Example trace showing a whole-cell recording of a CA3 PC (top) with simultaneous total power (0.3-80 Hz) of the nearby LFP (middle). Previously detected theta events are shown in grey since they were excluded from being classified as LIA states. Blue trace superimposed on the raw Vm is the smoothed Vm after spike removal. Bottom: two examples of Vm modulation during LIA events. (B) Spectrogram of the average LFP (z-scored within frequency bands) triggered by transitions to LIA (time = 0, dotted line) showing an increase in broadband power after the start of LIA. Middle: Average Vm traces during theta onset of an example hyperpolarizing (blue) and depolarizing (red) cell, as well as the grand average over all events (grey) (n = 403, shaded areas represent ± sem). Bottom: Color plot showing the Vm of CA3 PCs triggered by transition to LIA normalized to 4 to 2 s before start of LIA. Blue represents Vm hyperpolarization, red Vm depolarization. Each cell is represented in between black ticks. Cells are ordered depending on their Vm modulation during LIA, with depolarizing cells on top and hyperpolarizing cells at the bottom of the plot. Events within each cell are ordered by the time in which they occurred in the recording. Red vertical line indicates the sample cell shown in the average traces above. (C) Distribution of the magnitude of change in Vm at the onset of LIA (n = 403 events, bin size = 0.5 mV). Inset: pie chart of the different event types (18.9% hyperpolarizing [n = 76 events], 43.9% depolarizing [n = 177 events], 37.2% no change [n = 150 events]). Compared to a shuffled data set, there were significantly fewer hyperpolarizing events ($p < 0.001$) and more depolarizing events ($p < 0.001$) than expected by chance. (D) Distribution of cells' average Vm change during LIA (bin size = 1 mV). Inset: pie chart of the different cell types (9 cells were depolarizing and 25 cells showed no significant modulation towards one specific direction). (E) Comparison of direction of Vm modulation during theta versus LIA events. Left: example trace showing a whole-cell recording of a CA3 PC during LIA and theta. Right: Average change in Vm during theta versus average change in Vm during LIA. Filled circles represent significant modulation during LIA, and color represents direction of modulation.

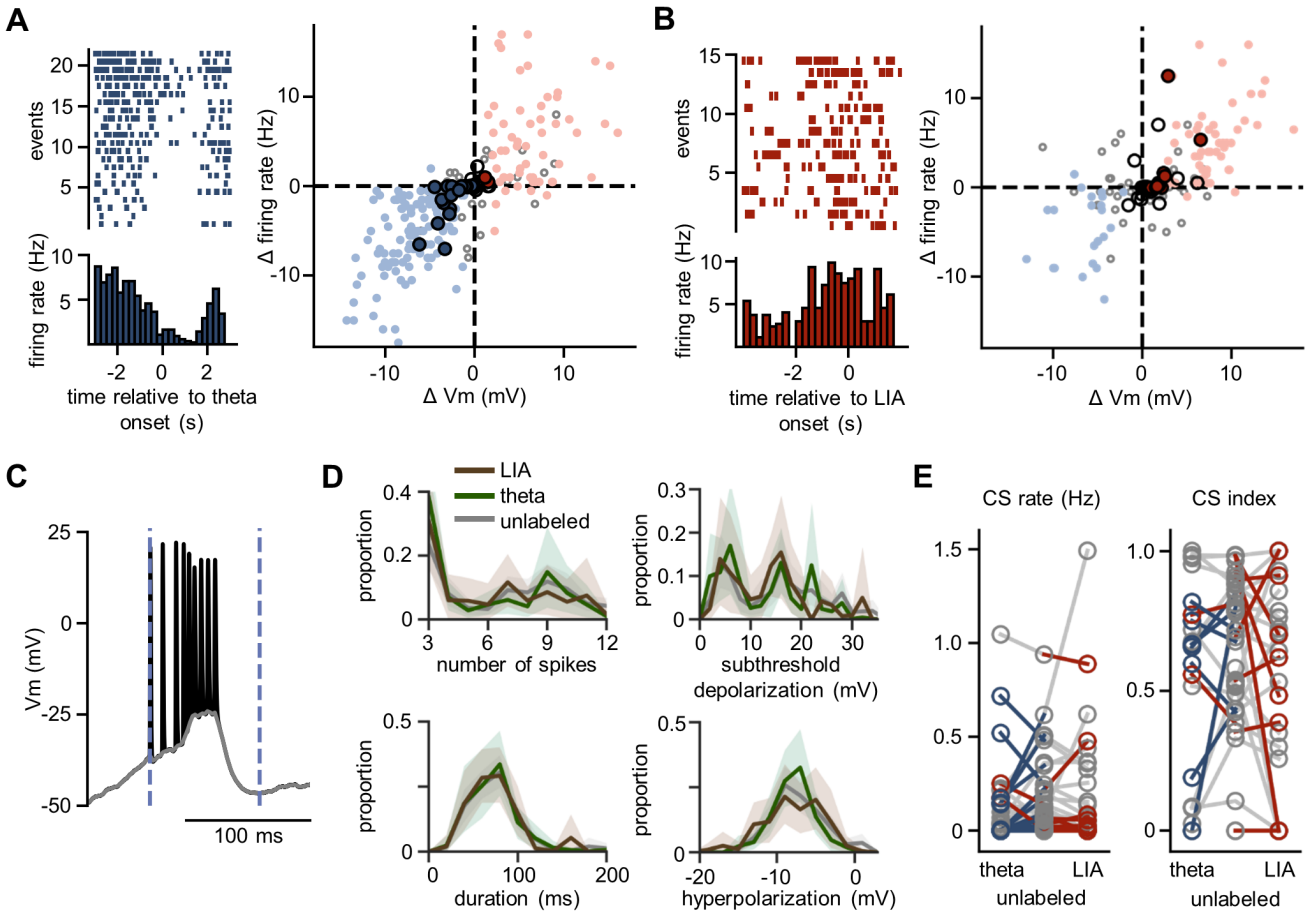
A
events
firing rate (Hz)
time relative to theta onset (s)
Δ firing rate (Hz)
Δ Vm (mV)
B
events
firing rate (Hz)
time relative to LIA onset (s)
Δ firing rate (Hz)
Δ Vm (mV)
C
Vm (mV)
100 ms
D
LIA
theta
unlabeled
proportion
number of spikes
subthreshold depolarization (mV)
duration (ms)
hyperpolarization (mV)
E
CS rate (Hz)
CS index
theta
LIA
unlabeled

Figure 5. State-associated change in Vm is associated with corresponding changes in firing rate. (A) Firing rate of CA3 PCs during theta. Left: raster plot (top) and peri-stimulus time histogram (PSTH, bottom) showing the firing activity of a significantly hyperpolarizing cell. In the raster plot, a single tick represents a single spike and each line is a transition to theta triggered at time 0. The PSTH represents the firing rate of the same cell for all theta transitions triggered at time 0. Right: mean change in firing rate versus mean change in Vm during theta. Large dots represent average changes for a single cell (n = 35 cells). Small dots represent single event (n = 223 events). Filled dots represent significant Vm modulation during theta, color represents the direction of modulation (B) As in (A) but for LIA (n = 34 cells or 115 events). (C) Example trace showing a representative CS. Blue dotted lines represent beginning and end of the CS used to calculate CS duration and amplitude of subthreshold depolarization and after hyperpolarization. Grey line represents the subthreshold membrane potential. (D) CS properties for each state; distributions are separate by state and averaged over cells. Top left: number of spikes per CS (7 ± 3.0 spikes [n = 31 cells] for unlabeled, 6.8 ± 2.6 spikes [n = 18 cells] for theta, 6.8 ± 2.7 spikes [n = 20 cells] for LIA, paired test over cells: p = 0.549 for theta vs unlabeled, p = 0.065 for LIA vs unlabeled). Top right: subthreshold depolarization under CS (16.8 ± 7.5 mV [n = 31 cells] for unlabeled, 13 ± 5.9 mV [n = 18 cells] for theta, 14.5 ± 5.2 mV [n = 20 cells] for LIA, paired test over cells: p = 0.149 for theta vs unlabeled, p = 0.208 for LIA vs unlabeled). Bottom left: CS duration (82.3 ± 18 ms [n = 31 cells] for unlabeled, 82.8 ± 16 ms [n = 18 cells] for theta, 76.6 ± 17.3 ms [n = 20 cells] for LIA, paired test over cells: p = 0.856 for theta vs unlabeled, p = 0.010 for LIA vs unlabeled). Bottom right: after-CS hyperpolarization (-6.5 ± 1.8 mV [n = 31 cells] for unlabeled, -7.2 ± 1.5 mV [n = 18 cells] for theta, -7.1 ± 2.1 mV [n = 20 cells] for LIA, p = 0.015 for theta vs unlabeled, paired test over cells: p = 0.435 for LIA vs unlabeled). (E) CS rate and CS index for theta, unlabeled and LIA events. Color represents significant Vm modulation during each state. The CS rate is lower during theta than during unlabeled, but there is no difference between unlabeled and LIA (0.01 ± 0.12 Hz [n = 35 cells] for theta, 0.03 ± 0.17 Hz [n = 34 cells] for LIA, 0.08 ± 0.14 Hz [n = 35 cells] for unlabeled, p = 0.037 for theta vs unlabeled, p=0.686 for LIA vs unlabeled). The CS index does not significantly differ between states for cells in which a CS index could be calculated (0.66 ± 0.28 [n = 20 cells] for theta, 0.63 ± 0.31 [n = 26 cells] for LIA, 0.72 ± 0.23 [n = 33 cells] for unlabeled, p = 0.053 for theta vs unlabeled, p=0.129 for LIA vs unlabeled).

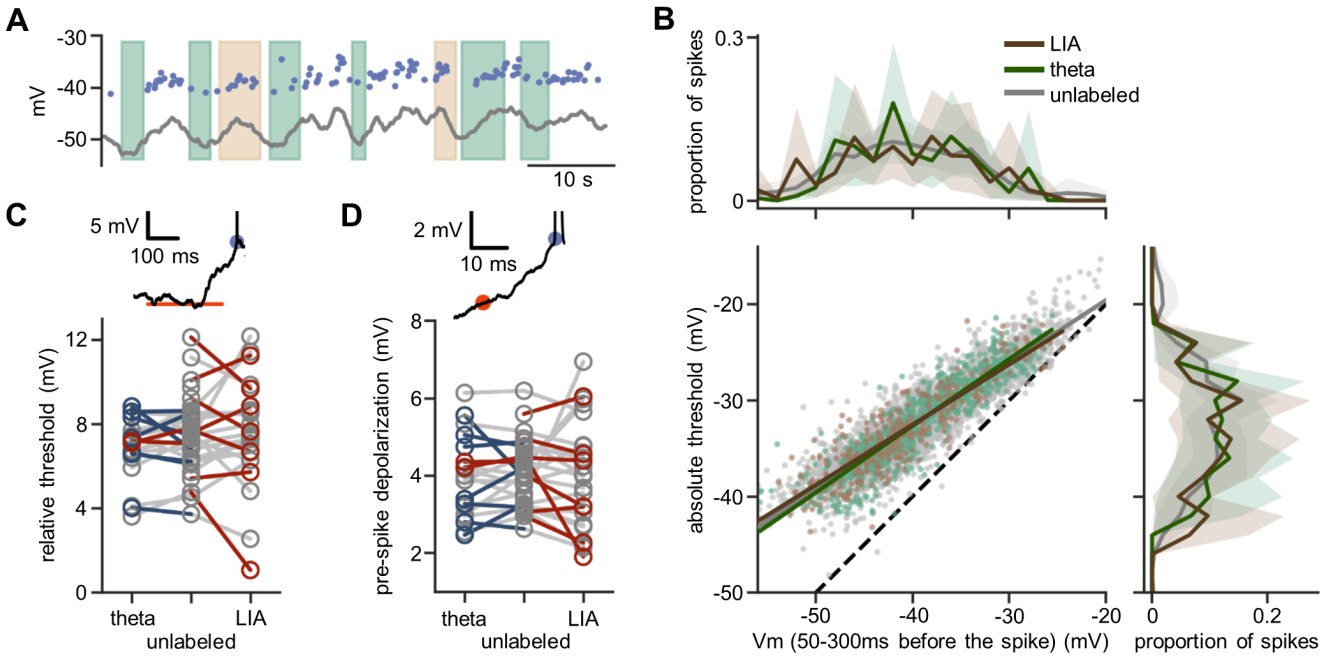
A
-30
-40
-50
mV
10 s
B
0.3
0
proportion of spikes
LIA
theta
unlabeled
-20
-30
-40
-50
absolute threshold (mV)
-50
-40
-30
-20
Vm (50-300ms before the spike) (mV)
0
0.2
proportion of spikes
C
5 mV
100 ms
12
8
4
0
relative threshold (mV)
theta
LIA
unlabeled
D
2 mV
10 ms
8
6
4
2
pre-spike depolarization (mV)
theta
LIA
unlabeled

Figure 6. Dynamic changes in spike threshold relative to membrane potential. A. Example trace showing smoothed Vm (grey line) and spike thresholds (blue dots). Shaded areas represent states. (B) Bottom left: Absolute spike threshold vs baseline Vm value 50-300 ms before the spike. Dots represent single spikes, color represents the state in which the spike occurs. The correlations were not significantly different between states ($y = 0.66x – 6.5$ for unlabeled [n = 3731 spikes], $y = 0.69x – 4.9$ for theta [n = 895 spikes], $y = 0.63x – 7.5$ for LIA [n = 328 spikes]. ANCOVA, $p = 0.142$). Top: Histograms of the baseline Vm prior to spikes, separated by state and averaged over cells (-38.7 ± 5.1 mV [n = 33 cells] for unlabeled, -39.2 ± 4.6 mV [n = 20 cells] for theta, -40.4 ± 6.1 mV [n = 26 cells] for LIA, paired test over cells: $p = 0.604$ for theta vs unlabeled, $p = 0.011$ for LIA vs unlabeled). Right: Histograms of the spike threshold, separated by states and averaged over cells (-31.5 ± 4.32 mV [n = 33 cells] for unlabeled, -31.2 ± 4.1 mV [n = 20 cells] for theta, -33.0 ± 4.7 mV [n = 26 cells] for LIA, paired test over cells: $p = 0.672$ for theta vs unlabeled, $p < 0.001$ for LIA vs unlabeled). (C) Top: example spike (truncated) showing the absolute spike threshold (purple dot) and the Vm 500-300 ms before the spike (orange line). Bottom: Relative threshold (difference between absolute spike threshold and baseline Vm) for each cell during theta, LIA and unlabeled states. Color represents significant Vm modulation during the state. There was no significant difference in the relative threshold over states (7.16 ± 1.05 mV [n = 20 cells] for theta, 7.55 ± 1.76 mV [n = 25 cells] for LIA, 7.62 ± 1.31 mV [n = 33 cells] for unlabeled, $p = 0.157$ for theta vs unlabeled, $p=0.645$ for LIA vs unlabeled). (D) Top: example spike (truncated) showing the absolute spike threshold (purple dot) and the Vm 20 ms before the spike (orange dot). Bottom: Same as (C) but for the pre-spike depolarization. There was no significant difference in the pre-spike depolarization over states (3.94 ± 0.82 mV [n = 20 cells] for theta, 4.03 ± 1.11 mV [n = 25 cells] for LIA, 4.03 ± 0.65 mV [n = 33 cells] for unlabeled, $p = 0.339$ for theta vs unlabeled, $p=0.430$ for LIA vs unlabeled).

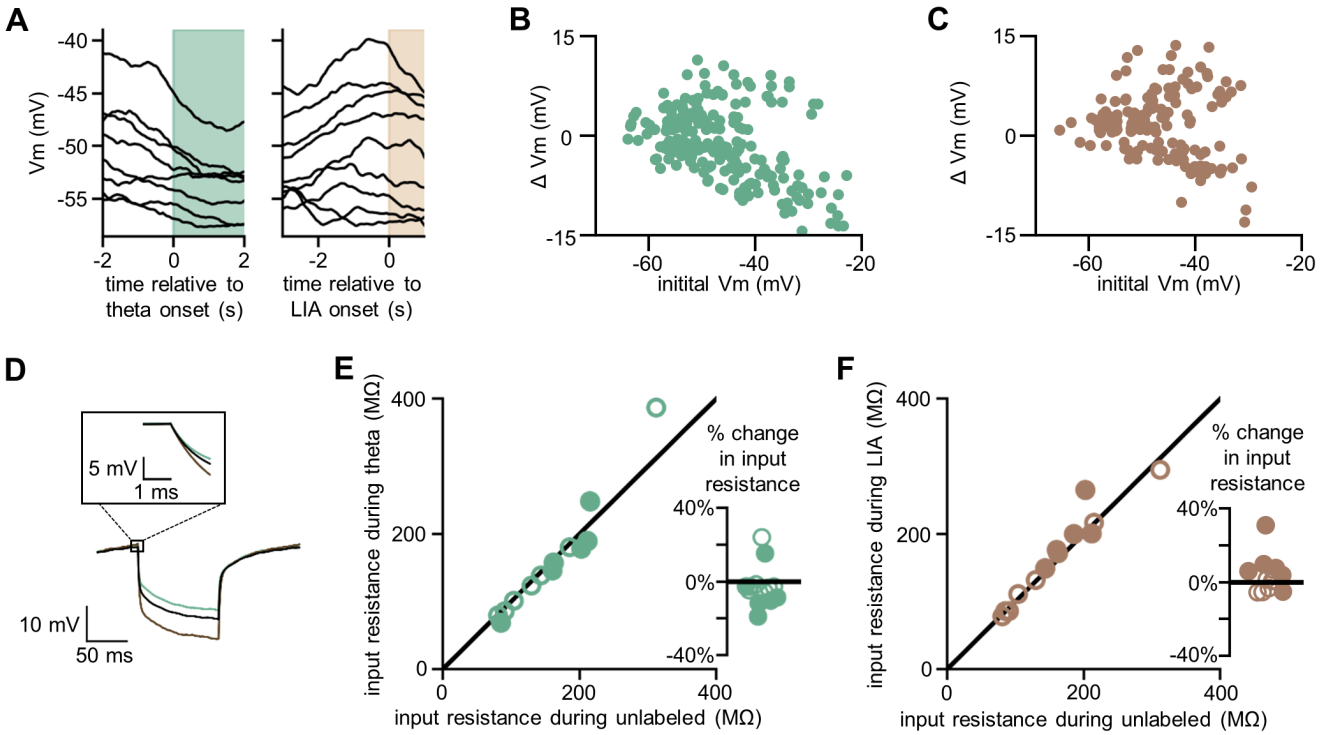
A
Vm (mV)
-40
-45
-50
-55
-2
0
2
time relative to theta onset (s)
-2
0
time relative to LIA onset (s)
B
Δ Vm (mV)
15
0
-15
-60
-40
-20
initital Vm (mV)
C
Δ Vm (mV)
15
0
-15
-60
-40
-20
initital Vm (mV)
D
5 mV
1 ms
10 mV
50 ms
E
input resistance during theta (MΩ)
400
200
0
0
200
400
input resistance during unlabeled (MΩ)
% change in input resistance
40%
0%
-40%
F
input resistance during LIA (MΩ)
400
200
0
0
200
400
input resistance during unlabeled (MΩ)
% change in input resistance
40%
0%
-40%

Figure 7 – Initial membrane potential and input resistance of CA3 PCs during brain states. (A) Left: example traces showing Vm modulation during theta for different initial Vm values in a single cell. Right: same but for LIA. (B) Vm changes during theta (ΔVm) versus the initial membrane potential (initial Vm) of the cell [n = 218 events]. (C) Same as in (B) but for LIA [n = 144 events]. (D) Average voltage response to current pulses (-100 pA, 100 ms) in an example cell during theta (green), LIA (brown) and no-state (black). Inset: zoom in at the onset of the current pulse. (E) Input resistance during theta versus unlabeled for the subset of cells for which resistance measurements were taken (n = 13 cells). Filled circle represents significance, Inset: Percentage change in input resistance during theta compared to unlabeled (-3.4% ± 6.9%, p = 0.491). (F) Same as in (E) but for LIA (1.5% ± 6.4 %, p = 0.874).

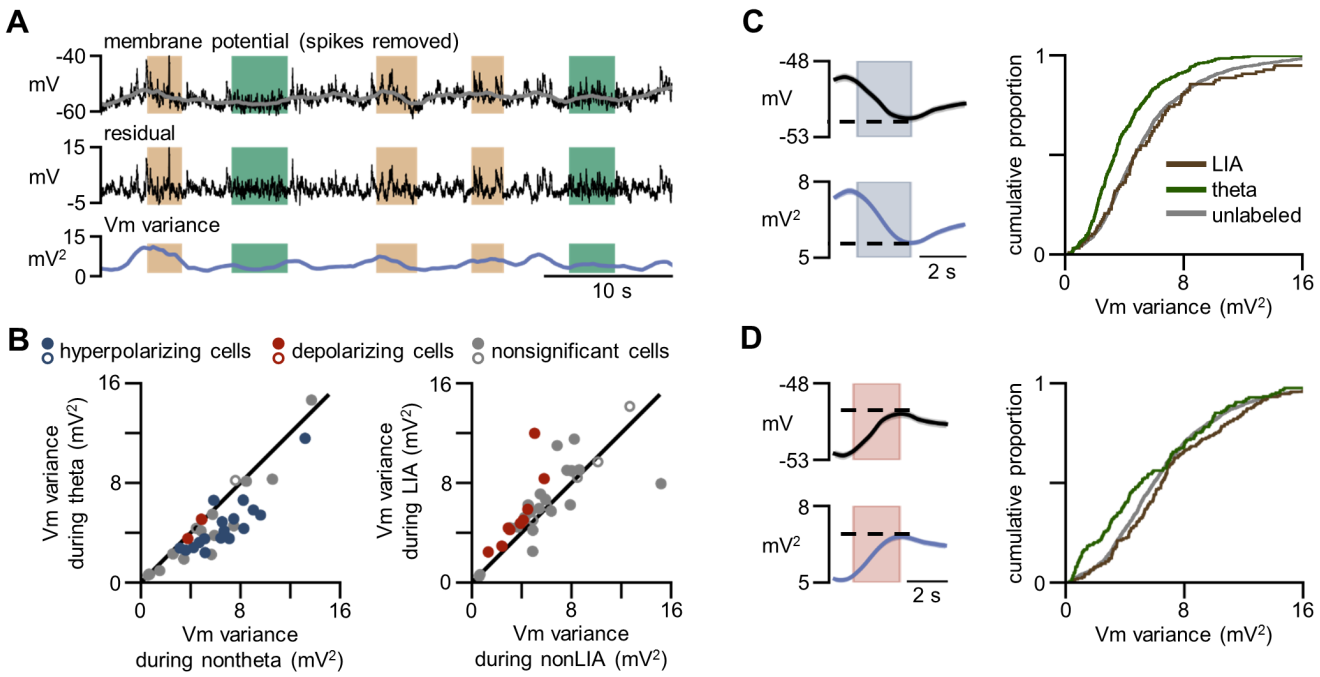
A
membrane potential (spikes removed)
-40
mV
-60
residual
15
mV
-5
Vm variance
15
mV2
0
10 s
B
hyperpolarizing cells
depolarizing cells
nonsignificant cells
Vm variance during theta (mV2)
Vm variance during nontheta (mV2)
Vm variance during LIA (mV2)
Vm variance during nonLIA (mV2)
16
8
0
C
-48
mV
-53
8
mV2
5
2 s
cumulative proportion
1
LIA
theta
unlabeled
Vm variance (mV2)
D

Figure 8 - Variance of membrane potential of CA3 PCs is low during theta and high during LIA. (A) Processing of Vm trace to measure its variance. Top: downsampled Vm after spike removal of a CA3 PC with shading indicating theta (green) and LIA (brown). The grey superimposed trace is after smoothing with a window of 2 seconds. The smoothed Vm is subtracted from the spike-removed Vm to obtain the residual Vm (middle). The variance of the residual Vm trace is calculated over 1-second windows (bottom). (B) Left: scatter plot showing Vm variance of each cell during theta versus nontheta (n = 35 cells). Filled dots represent a significant difference in variance. Over the population of cells, there was a significant decrease in variance during theta (5.73 ± 2.25 mV^2 for nontheta, 4.15 ± 1.98 mV^2 for theta, mean difference = -1.41 mV^2, $p < 0.001$). Color represents direction of modulation during theta (blue: significantly hyperpolarizing cell: red: significantly depolarizing cell: grey: nonsignificant change), and filled dots represent a significant difference in variance between theta and nontheta. Right: same, but for LIA. Over the population of cells, there was a significant increase in variance during LIA (4.96 ± 2.22 mV^2 for nonLIA, 5.92 ± 2.36 mV^2 for LIA, mean difference = 0.74 mV^2, p = 0.022). (C) Left: Average of all hyperpolarizing events Vm (top, black) and variance (bottom, blue, n = 1783 events). Dotted line corresponds to the value taken at the end of the change in Vm for each event. Right: Cumulative proportion of variance during LIA (brown), theta (green) and unlabeled (grey) hyperpolarizing events. Vm variance is lower during theta and higher during LIA(3.39 ± 1.86 mV^2 [n = 388 events] for theta, 4.77 ± 3.05 mV^2 [n = 98 events] for LIA, 4.77 ± 2.75 mV^2 [n = 1301 events] for unlabeled, $p < 0.001$ for theta vs unlabeled and theta vs LIA, p = 0.006 for LIA vs unlabeled). (D) Left: Average of all depolarizing events Vm (top, black) and variance (bottom, blue, n = 1871 events). Dotted line corresponds to the value taken at the end of the change in Vm for each event. Right: Cumulative proportion of variance during LIA, theta and unlabeled depolarizing events. Vm variance is lower during theta but there is no difference between LIA and unlabeled depolarizations (5.18 ± 3.76 mV^2 [n = 173 events] for theta, 6.56 ± 3.57 mV^2 [n = 194 events] for LIA, 6.11 ± 3.52 mV^2 [n = 1507 events] for unlabeled, p = 0.021 for theta vs unlabeled, p=0.017 for theta vs LIA, p = 0.205 for LIA vs unlabeled).